Analysis of the impact of optical aberrations in en-face full-field OCT microscopy

Marie Blavier, Marie Glanc, Gérard Rousset

Research Article | Vol. 29, No. 2 / 18 January 2021 / Optics Express 2204
Optics EXPRESS

Analysis of the impact of optical aberrations in en-face full-field OCT microscopy

MARIE BLAVIER, MARIE GLANC,* AND GÉRARD ROUSSET

LESIA, Observatoire de Paris, Université PSL, CNRS, Sorbonne Université, Université de Paris, 5 Place Jules Janssen, 92195 Meudon, France
*marie.glanc@obspm.fr

Abstract: Optical coherence tomography (OCT) is a powerful technique for cross-sectioning imaging. However, the lateral resolution may be degraded by optical aberrations originating from the sample or the setup. We present an extensive quantitative study of the impact of aberrations in time-domain en-face full-field OCT (FFOCT). Using an adaptive optics loop integrated in an FFOCT setup, a deformable mirror is used to introduce low-order calibrated aberrations. The experimental analysis of both the line spread functions (SF) and the complex object images has allowed us to measure the loss in contrast and the impact on lateral spatial resolution. We demonstrate that the frequency content of FFOCT image spectra in terms of signal-to-noise ratio and cutoff frequency is degraded by aberrations but remains much higher than in conventional incoherent images. Line SF profiles in conventional imaging display widening, whereas in FFOCT they display oscillations, leading to the possible perception of preserved resolution. Nevertheless, for complex objects, the aberration image blurring is strong due to the convolution process by the point SF, resulting in a significant filtering of the image spatial spectrum.

1. Introduction

Optical coherence tomography (OCT) is a technique for cross-sectional imaging based on interferometry [1–3]. OCT is particularly praised by ophthalmologists, and different kinds of OCT devices are already commercially available for applications in this medical field. Indeed, they facilitate the noninvasive rapid examination of the integrity of the different layers of the retina.

Given that the eye exhibits optical aberrations of both low and high order that fluctuate over time [4], the acquisition of x-y high-resolution images of the retina is a challenge that can be partially mitigated by using Adaptive Optics (AO) [5,6]. Originating from astronomy [7,8], this technique is well adapted to the correction of 2D en-face images. Nevertheless, it does not facilitate sufficient sectioning if used in a standard "Laser Guide Star AO" astronomical configuration [9], even if the eye's aberrations are primarily located close to the pupil. Moreover, full-field OCT (FFOCT) can directly acquire en-face images (thus obviating the necessity to implement a relatively slow, and potentially distorting x-y scan), the z-resolution of which is essentially linked to the temporal coherence length of the imaging source [10]. Coupling both techniques to obtain x-y-z high-resolution images of the retina by integrating an AO loop in the sample arm of the interferometer is of great interest [11].

FFOCT is based on a Linnik configuration, and was initially developed to achieve high lateral resolution by using high numerical aperture (NA) microscope objectives at the end of both arms [12,13]. In ophthalmology, using FFOCT to perform real-time contactless imaging of the human cornea has resulted in the development of new promising diagnostic tools [14]. However, when used alone, in some configurations (for retinal imaging), optical aberrations may lead to a decrease in performance. Aberrations can adversely affect FFOCT images in two ways. First, they reduce interferometric contrast. As a result, the signal-to-noise ratio (SNR) of the FFOCT signal is reduced. Depending on the application, it may be necessary to perform aberration

#403432 https://doi.org/10.1364/OE.403432
Journal © 2021 Received 22 Jul 2020; revised 26 Nov 2020; accepted 26 Nov 2020; published 13 Jan 2021

Optics EXPRESS

correction. Second, aberrations can cause a decrease of the 2D spatial resolution by broadening the point spread function (PSF), thereby reducing the high spatial frequency content.

The impact of aberrations on FFOCT images was investigated by Xiao et al. [15,16]. They concluded that the FFOCT spatial resolution is almost insensitive to aberrations. However, they only considered relatively small aberration amplitudes and point-like diffuser images in their study. They also acquired *in vivo* retinal images of the photoreceptor mosaic in a healthy subject using a custom-built FFOCT setup at 6° of eccentricity [17]. Recently, Mecê et al. improved this implementation and obtained photoreceptor images in a healthy subject at smaller eccentricities [18]. The images are impressive, with well-resolved cones. However, additional information on the associated aberrations would be of great value. The main question is: "Do aberrations have an effect on the quality of FFOCT images of biological tissue?"

In this report, we address this question by exploiting our FFOCT experimental bench, including an adaptive optics deformable mirror. We analyze and quantify the FFOCT image quality of various objects in terms of the achieved contrast and spatial resolution, depending on the nature and amplitude of the aberrations. Relying on the equations that describe the image formation processes in conventional incoherent imaging and FFOCT, we propose an explanation for the specific manifestations of resolution loss in the images.

We have developed a platform based on FFOCT, which includes AO compensation in the sample arm of the interferometer. The initial purpose is to perform 3D high-resolution imaging of *ex vivo* samples, especially of retina samples. Using the AO in open loop, calibrated aberrations can be introduced using the deformable mirror, and their impact on the FFOCT signal can be analyzed. In Section 2, we theoretically describe the image formation process in our FFOCT setup. In Section 3, we introduce the setup used to perform the study. Section 4 summarizes the methodology used to acquire the FFOCT images with different aberrations, measure the contrast, and quantify the impact of the aberrations. In Section 5, we present the results obtained for various samples and provide an explanation of the image properties by examining the spatial frequency content obtained for the different samples. Following the main conclusions, a theoretical expression for the FFOCT image is presented in the Appendix in addition to the derivation of the cutoff frequency in FFOCT.

2. Theoretical assessment

In this section, we introduce the theoretical formulation of the signal used for the analysis of our FFOCT experiment (Fig. 1).

To compute an OCT image, we first record four interferograms ($I_{\Delta\varphi}$), each with a different phase shift $\Delta\varphi$ that is introduced in the reference arm of the interferometer (Section 3). The four-phase shifts $\Delta\varphi$ are 0, $\pi/2$, π, and $3\pi/2$. Then, the computed OCT image $I^2_{OCT\_comp}$ is derived based on the recorded intensities of the phase-shifted interferograms as follows:

$$I^2_{OCT\_comp} = (I_0 - I_\pi)^2 + (I_{\pi/2} - I_{3\pi/2})^2. \tag{1}$$

We also must consider the impact of noise on the OCT images. To account for noise, the detected interferograms $I^d_{n\pi/2}$ ($n = 0, 1, 2, or\ 3$) are represented as follows:

$$I^d_{n\pi/2} = I_{n\pi/2} + \eta_{n\pi/2}, \tag{2}$$

where $I_{n\pi/2}$ is the mean intensity of the interferogram and $\eta_{n\pi/2}$ is the noise (a centered random variable). Introducing $I^d_{n\pi/2}$ in Eq. (1) and after averaging for several draws, we can express the computed OCT image as follows:

$$\left\langle I^2_{OCT\_comp} \right\rangle = I^2_{OCT} + \left\langle \eta^2_0 \right\rangle + \left\langle \eta^2_{\pi/2} \right\rangle + \left\langle \eta^2_\pi \right\rangle + \left\langle \eta^2_{3\pi/2} \right\rangle, \tag{3}$$

Optics EXPRESS

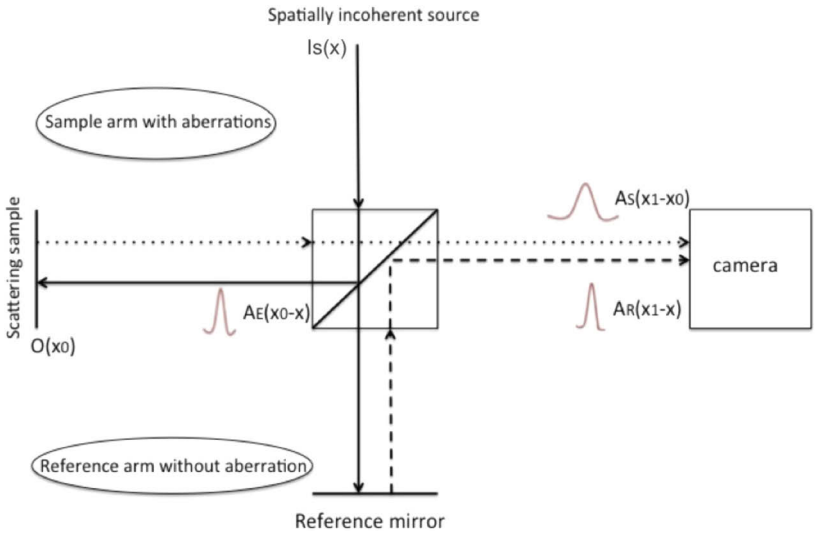

Fig. 1. Schematic view of the interferometer with the impulse responses expressed as field amplitude for both arms and a source intensity of $I_s(x)$.

Where I^2_{OCT} is the sought OCT image of the object and $<\eta^2_{n\pi/2}>$ is the noise contribution from the 4 interferograms. In this equation, we see that noise is a bias term in the computed OCT image [19]. Let us emphasize that for a very large number of draws, the noise terms converge to the sum of the four noise variances (which is equal to four times the noise variance in one interferogram when the noise is dominated by the incoherent intensity photon noise).

In the Appendix, we develop an approximate expression for the OCT image I^2_{OCT} based on the fields diffracted by the two arms of the interferometer and the spatial incoherence of the illumination source, assuming only surface scattering on the imaged object. We thus obtain:

$$I^2_{OCT}(x_1) = 16\left|\int\left(\int^{I_S}(x)A_E(x_0-x)A^*_R(x_1-x)dx\right)A_S(x_1-x_0)O(x_0)dx_0\right|^2, \tag{4}$$

where (Fig. 1 illustrates the different signals):

- $I_S(x)$ is the mean intensity emitted by the source point at coordinate x;
- we use the three following diffracted field amplitude impulse responses to characterize light propagation in the instrument:
  - $A_E(x_0 - x)$ the field amplitude that illuminates the object at the point x_0 for an emitting source point at coordinate x (propagation in the sample arm towards the object),
  - $A_R(x_1 - x)$ the amplitude at the image point for coordinate x_1 from the reference arm for a source point at coordinate x,
  - $A_S(x_1 - x_0)$ the amplitude at the image point of coordinate x_1 for the wave scattered by the object point at x_0 (propagation in the sample arm towards the detection plane);
- $O(x_0)$ is the object reflection coefficient amplitude for the scattering point at coordinate x_0.

The coordinates x, x_0, and x_1 have their origin in the center of the image plane.

Equation (4) shows that the OCT image is based on an integral term that is similar to the convolution of the object's reflection coefficient $O(x_0)$ and the instrument response that links the

Optics EXPRESS

source intensity and the different diffracted field amplitudes. In our configuration, both A_E and A_S have aberrations that are introduced in the sample arm, whereas A_R is free of aberration since it represents the signal for the reference arm.

Two limit cases can be considered First, when A_R is assumed to be close to a Dirac function (for a very large pupil), we have

$$I_{OCT}^2(x_1) \approx 16\left|I_S(x_1)\int A_E(x_0 - x_1)A_S(x_1 - x_0)O(x_0)dx_0\right|^2. \quad (5)$$

The instrument response is given by the amplitude product $A_E(x_0 - x_1)A_S(x_1 - x_0)$, which includes all the aberrations of the sample arm, resulting in a blurred OCT image of the object. This shows that the aberrated illumination of the sample must be considered in the image computation process.

Second, when A_E is assumed to be close to a Dirac function (non-aberrated and very large pupil illumination of the object), we obtain the following:

$$I_{OCT}^2(x_1) \approx 16\left|\int A_R^*(x_1 - x_0)A_S(x_1 - x_0)I_S(x_0)O(x_0)dx_0\right|^2. \quad (6)$$

The instrument response is given by the amplitude product $A_R^*(x_1 - x_0)As(x_1 - x_0)$ resulting in a much less aberrated response and possible preservation of the spatial resolution, driven by A_R, in the OCT image of the object.

From these two limit cases, we can conclude that the aberrated illumination of the sample contributes to the possible degradation of the resolution in the FFOCT image, and that the potential preservation of the resolution is linked to the aberration-free reference arm amplitude.

3. FFOCT setup

The time-domain FFOCT we developed is based on a Linnik interferometer (Fig. 2), with microscope objectives used to focus a light beam onto a plane mirror (reference arm) and onto the sample (sample arm). It consists of 4 paths. The source arm defines the field and pupil planes. The reference arm is composed of a microscope objective (Olympus MPLFLN10XBDP) and a plane reference mirror mounted on a piezoelectric transducer (PZT; S.303-CD, Physics Instruments). Both the microscope objective and reference mirror are mounted on a Newport M-UTM25PP1HL motorized stage, whereas the reference mirror and the PZT are mounted on a Newport M-VP-25XA motorized stage. The sample arm includes the AO loop: an ALPAO 97 magnetic actuator deformable mirror is located in a pupil plane. The sample was mounted on a Newport LTA-HS motorized plate, with the microscope objective (Olympus UMPLFLN10XW) kept static. With an effective numerical aperture smaller than 0.2, this water immersion objective can also be used in air with good optical quality. The detection arm contains a CCD camera (Hamamatsu C9100; 1000×1000 pixels; 8 µm pixel size; Shannon sampling for a 7 mm diameter pupil in conventional imaging) for the acquisition of the interferograms. Masking the reference arm allows one to acquire incoherent conventional images of the sample. To separate the arms, we use a polarized beam splitter cube. In combination with quarter-wave plates, this facilitated the removal of most of the spurious back reflections of the optical components, which may otherwise increase the incoherent noise in the setup. This is particularly important when imaging objects with a low level of coherent signal such as the retina.

Two modes of z-scans are available using our setup: scanning by moving the sample itself (most *ex vivo* cases) or not (as will be the case for *in vivo* samples). For the *ex vivo* configuration, the surface of the sample can be z-aligned with the surface of the reference mirror at the beginning of the scan in an optical conjugation. Then, the sample is moved by a chosen value to perform the z-scan. For each imaging depth, motorized stages are used to maintain coincidence between

Optics EXPRESS

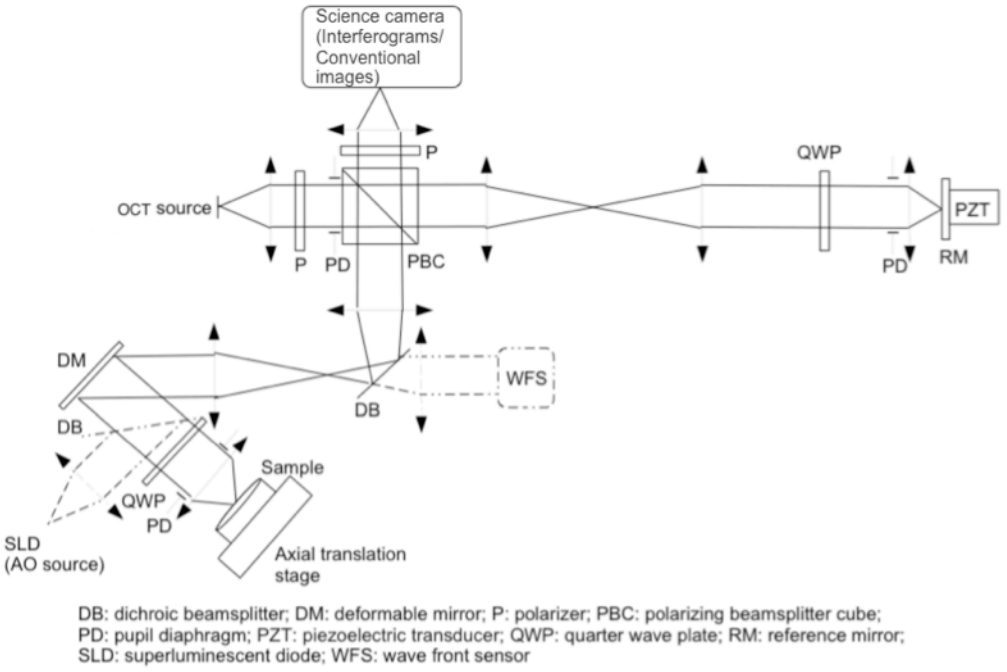

Fig. 2. FFOCT setup based on a Linnik interferometer. Dashed line: AO setup (SLD source + wavefront sensor). For simplification, all lenses are not shown: afocal telescopes ensure pupil and field conjugations.

the zero optical-path-difference (OPD) plane and the focal plane (contrast maximization, no uncontrolled lagging defocus). Four 2D-interferograms are then acquired using the CCD camera, each corresponding to a calibrated PZT shift, to introduce the appropriate phase shift.

The OCT illumination source is an LED ($\lambda = 730$ nm; $\Delta\lambda = 37$ nm; Thorlabs M730L4) based on a Köhler illumination scheme. The field-of-view (FOV) can reach 960 µm in the focal plane of the sample arm objective. In the setup, the diameter of most of the pupils can be independently tuned, with a maximum value of 7 mm. Unless indicated, they are set equal to 5 mm for the presented results.

For this pupil size, the reference arm is mostly without aberrations, as seen in the PSF of Fig. 3**.** Wavefront error measurement was performed once, when the arm was aligned, reaching less than $\lambda/14$ for a 5 mm pupil (one way, without a microscope objective in place). This measurement, obtained through a Haso 32 Imagine Optic wavefront sensor, appears to be compatible with the "outward and return PSF" (presence of the reference microscope objective at the end of the arm) displayed in Fig. 3. We estimate a PSF full-width at half-maximum (FWHM) that is very close to the diffraction limit. The first bright ring of the diffraction pattern is observed, and the second one is partially detected.

In this study, a deformable mirror (DM) is used to compensate for the aberrations of the sample arm and to introduce selected aberrations in a pupil plane that is conjugated with the objective pupil plane. Without the introduction of the DM aberrations, the optical quality of the sample arm after compensation was estimated to be on the order of $\lambda/20$ at the imaging wavelength. The amount of applied DM aberrations was determined using a custom-built Shack–Hartmann wavefront sensor that was designed for ocular aberration correction (tunable number of sub-apertures depending on the desired pupil size; 18×18 sub-apertures corresponding to 7 mm pupil diameter; 12×12 pixels per sub-aperture; 1.8 pixels per diffraction-limited sub-aperture spot

Optics EXPRESS

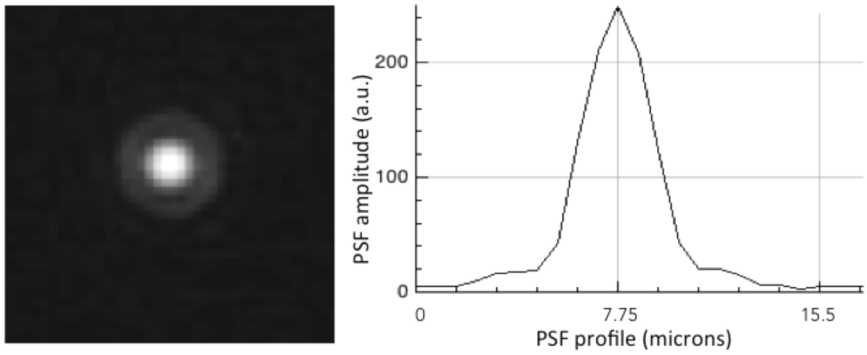

Fig. 3. Left: Oversampled and saturated PSF of the reference arm for 5 mm pupil (log scale to better see the first two Airy rings). Right: Linear profile of the corresponding non-saturated PSF. FWHM ~3 µm versus 2.7 µm theoretically. First bright ring radius ~4.3 µm in accordance with theory. Second bright ring radius ~6.6 µm compared with 7 µm theoretically.

FWHM; closed-loop frequency of 100 Hz). In addition, the aberration values were confirmed using a commercial wavefront sensor (HASO 32, Imagine Optic). The wavelength of the AO wavefront sensing was 830 nm, using a superluminescent diode (SLD 830S, Thorlabs) as a laser guide star. The DM is encountered on the outward optical path to the sample and the return path, resulting in aberrations that alter both the illumination of the sample and the backscattered light used to form its image on the camera.

4. Experimental methodology

In this study, calibrated aberrations were introduced in the sample arm pupil and FFOCT images were reconstructed. The transverse resolution and contrast of the FFOCT signal were measured for each aberration. The samples were either paper sheets, showing a large range of spatial frequencies, or a black diffusive painted sample containing small particles that acted as diffusers (as specified by the manufacturer) deposited on a metallic plate. This allowed us to mimic the scattering behavior in biological tissues (paint reference: NEXTEL velvet-coating 811-21).

4.1. Reference setting

First, we corrected for any static aberration in the sample arm by closing the AO loop of the DM with the wavefront sensor. This command applied to the DM was averaged over time and recorded as a calibration. The corresponding residual aberrations as measured by the wavefront sensor were less than 35 nm RMS (root mean square). We can consider the reference arm to be well aligned without any aberration (Fig. 3 for the corresponding PSF). Applying the DM calibrated command, we define a reference configuration. In this configuration, the FFOCT contrast and the resolution for each of the assessed samples were computed and used as reference values denoted hereafter as "without aberration."

4.2. Studied aberrations

We applied calibrated Zernike aberrations as offsets to the DM in the sample arm (reference arm remaining optically "perfect"). We use the Noll definition for the Zernike polynomial [20], ensuring that the generated aberrations modes are orthonormal. Only one Zernike polynomial is applied at a time. In particular, this means that the application of astigmatism, for instance, does not add any undesirable defocus. Given that these aberrations are directly generated using the DM in air, they are achromatic. Therefore, there was no direct impact on the coherence gating

Optics EXPRESS

performance (sectioning) of the OCT. The first Zernike modes (defocus, 3rd order astigmatism, 3rd order comas, 3rd third-order trefoils) were considered, and only some of them are selected for presentation in this report. Their amplitudes were selected between 0 and a few hundreds of nanometers, in a range compatible with measurements made on pathological or aging eyes [21,22]. The total value of the aberrations in micrometers RMS was determined by summing the square values of the corresponding Zernike coefficients, then taking the square root. This operation was performed using our real-time computer (RTC) that had previously been calibrated. The OCT image was reconstructed for each applied aberration, and the resolution and contrast were computed and compared to the reference value.

4.3. Measurement methods

4.3.1. FFOCT image acquisition and processing

In this section, the image acquisition and basic image processing are described. We acquired four interferograms using the camera for the four phase-shift values. Then, the OCT image is computed using Eq. (1). In practice, we systematically recorded $4N_{avg}$ interferograms to perform averaging and calculated $<I^2_{OCT\_comp}>$. We averaged N_1 interferograms classified by the phase shift, then averaged N_0 OCT images, where $N_1+N_0=N_{avg}$. Interferogram averaging facilitates the significant improvement of the signal-to-noise ratio [19], but it is particularly sensitive to vibrations. Therefore, careful data selection is necessary. OCT image averaging further increases the signal-to-noise ratio [19], without perturbation issues, but induces a bias.

Hence we have:

$$\left\langle I^2_{OCT\_comp} \right\rangle = \frac{1}{N_O} \sum_1^{N_O} \frac{1}{N_I^2} \left(\left(\sum_1^{N_I} (I_0 - I_\pi) \right)^2 + \left(\sum_1^{N_I} (I_{\pi/2} - I_{3\pi/2}) \right)^2 \right). \tag{7}$$

Considering our laboratory conditions, we selected N_1 and N_0 to be between 1 and 10. This image was normalized using a coefficient introduced to take into account possible source intensity fluctuations, to compensate for the reflection coefficient specific to each sample, and to make it directly comparable to a conventional image. This coefficient is given by

$$coeff = \frac{1}{2} \frac{1}{4N_{avg}} \sum_1^{N_{avg}} \left(I_0 + I_\pi + I_{\frac{\pi}{2}} + I_{\frac{3\pi}{2}} \right). \tag{8}$$

In Eq. (8), we introduce a ½ factor to directly compare the intensities obtained from FFOCT images and conventional ones (where no light comes from the reference arm). Finally, we compute all the FFOCT images in this report as:

$$I_{OCT} = \sqrt{\left\langle I^2_{OCT\_comp} \right\rangle} / coeff. \tag{9}$$

To evaluate the impact of the aberrations, we also analyzed the spatial frequency spectra derived from the OCT images. This is performed by first multiplying the image by a Hanning window W_H to avoid spurious oscillations in the spectra due to the image truncation. The window is defined as follows:

$$\begin{aligned} W_H(|x_1|) &= \frac{1}{2}(1 + cos(2\pi|x_1|/R)) \text{ for } |x_1| \le R, \\ W_H(|x_1|) &= 0 \text{for } |x_1| > R, \end{aligned} \tag{10}$$

where R is the half size of the image. The spatial spectrum of the image is then given by the modulus of the bi-dimensional Fourier transform:

$$Spectrum = |FT(I_{OCT} W_H)|. \tag{11}$$

Optics EXPRESS

To analyze such a spectrum, we generally plot a one-dimensional dependence by azimuthally averaging around the zero frequency.

To effectively compare the spectra for different aberrations, we also calibrated the noise level in the OCT images, using two methods. In the first approach, additional interferograms are recorded using only incoherent photons on an axially translated out-of-focus sample (to be completely out of the coherence zone). The calculation of I_{OCT} under these conditions is performed using Eqs. (7) to (11), which directly gives the noise level and noise spectrum. The 0-OPD signal (sample imaging) and large OPD signal (noise calibration) are computed using the same process (averaging, normalization. . .) at the same light illumination level.

The second method (used only in Section 5.3.2) is described as follows. Instead of calculating Eq. (1), we perform the following steps:

$$\begin{aligned} I^2_{OCT\_noise\_comp\_1} &= (I_{0,1} - I_{0,2})^2 + (I_{\pi/2,1} - I_{\pi/2,2})^2, \\ I^2_{OCT\_noise\_comp\_2} &= (I_{\pi,1} - I_{\pi,2})^2 + (I_{3\pi/2,1} - I_{3\pi/2,2})^2. \end{aligned} \tag{12}$$

$I_{\Delta\varphi,1}$ and $I_{\Delta\varphi,2}$ correspond to the first and second successive series of the 4 phase-shifted interferograms ($\Delta\varphi = 0$, $\pi/2$, π, and $3\pi/2$) respectively. This calculation provides the new first two OCT reconstructed images for noise calibration. We repeat the computation using Eqs. (12) for all successive couples of the series of interferograms. The ongoing process is based on Eqs. (8)–(11). This method has the benefit of relying on the same set of registered interferograms as those used to perform the OCT reconstruction. The disadvantage is that it is highly sensitive to small errors in $\Delta\varphi$ generated in successive recordings. These errors result in an imperfect subtraction of the common coherent part in the interferograms. As such, the reconstructed images still contain the signal and noise. The errors occur occasionally due to vibrations of the bench, and some of the reconstructed images cannot be kept in the calculations.

4.3.2. Conventional incoherent images

For conventional imaging, we simply masked the reference arm beam to record the sample images in a wide field mode (no sectioning). For the FFOCT images, we also normalized the images by their mean flux and computed the spatial spectra using the Hanning window. We calibrated the noise level in the conventional images by using a strongly defocused image to eliminate the object's signature. This way we kept the photon flux constant since photon noise is dominant in our images. The noise spectrum calculation procedure is similar to that of the signal.

4.3.3. Contrast measurement

Defining the fringe contrast on a given recorded interferogram as $(I_{max} - I_{min}) / (I_{max} + I_{min})$, one can show that this value is proportional to the reconstructed OCT image intensity I_{OCT}. We choose to consider the N brightest pixels from the OCT image and to average them to estimate the contrast value. Selecting only a portion of the brightest pixels in the image allowed us to minimize the impact of the noise bias in the contrast estimation process.

4.3.4. Resolution measurement

The resolution of the OCT system can first be qualitatively estimated by examining the reconstructed images. In addition, to allow for quantitative evaluation, the image spectra obtained via a Fourier transform of the OCT images were computed. This allowed us to compare the spatial frequency content as a function of the applied aberrations. Examination of the spectrum facilitated the evaluation of the change in resolution based on the different shapes of the curves as a function of the aberration, and potentially, a change in the experimental cutoff frequency. This method is well suited to the use of complex, extended, scattering objects such as biological samples. Alternatively, one can examine the spatial profiles of sharp edge images to compare

Optics EXPRESS

the impact of different aberrations on the process of image formation. This allowed us to obtain one-dimensional PSF-like images and to examine their evolution in terms of shape and width as a function of the aberrations.

5. Experimental results

5.1. Acquired images

FFOCT images were reconstructed with and without aberrations applied to the DM in the sample arm. Examples are given for the paper sheet (Fig. 4) and the diffusive painted sample (Fig. 5). The total FOV is 2.7° (845 pixels in the image diameter) and the CCD pixel corresponds to ~1 µm in the sample plane.

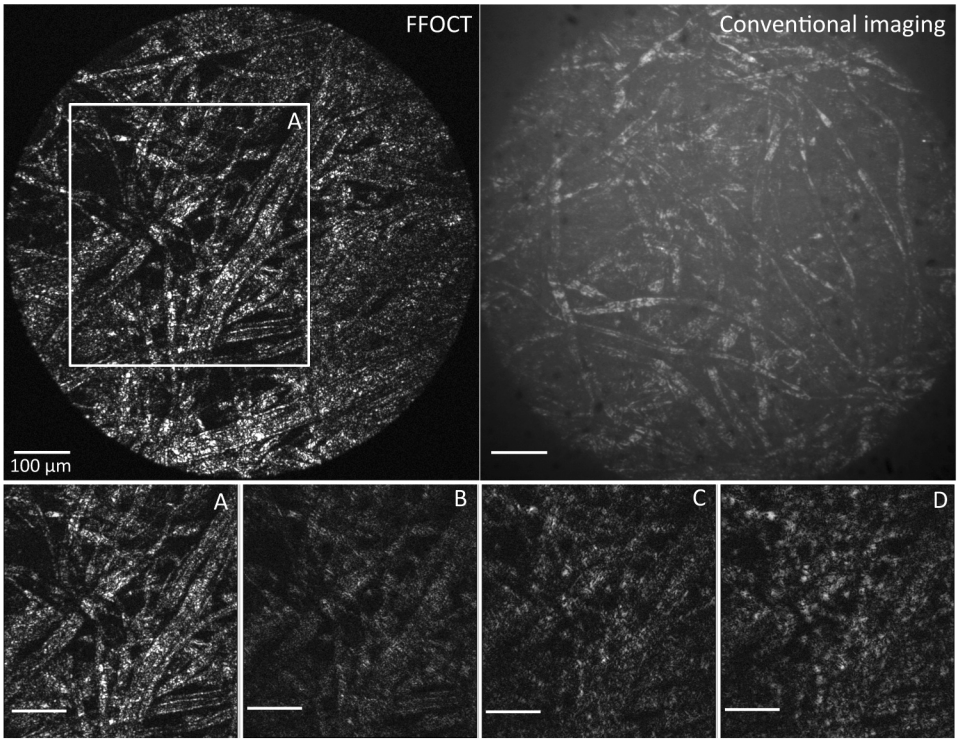

Fig. 4. FFOCT and conventional images at $\lambda = 730$ nm of a paper sheet. Top; the entire field-of-view (diameter: 845 µm) without aberration in FFOCT (left) and conventional (right) imaging. The square area selected for the bottom images (430 µm x 470 µm) is displayed in the FFOCT image. The conventional image was acquired using the same sample even though it does not present the same area as the FFOCT image. Bottom; FFOCT images with (A) no aberration, (B) 0.26 µm astigmatism, (C) 0.19 µm coma and (D) 0.19 µm trefoil. Image intensity extends over the entire dynamics of the camera. For A, B, C, and D, intensities are plotted using the same grey-level scale. Scale bar: 100 µm.

In Figs. 4 and 5, we observe the impact of aberrations in terms of contrast and deformations of the sample details in the FFOCT images, depending on the type of applied aberrations. Especially in Figs. 5(A), 5(B), 5(C), we can recognize some well-known structures of the expected PSF corresponding to the three considered aberrations on the bright "quasi point" scatterers of the sample.

If we examine the FFOCT images of a scattering continuous medium such as a paper sheet (Fig. 4), speckles dominate the images. However, the speckle width is not modified by the

Optics EXPRESS

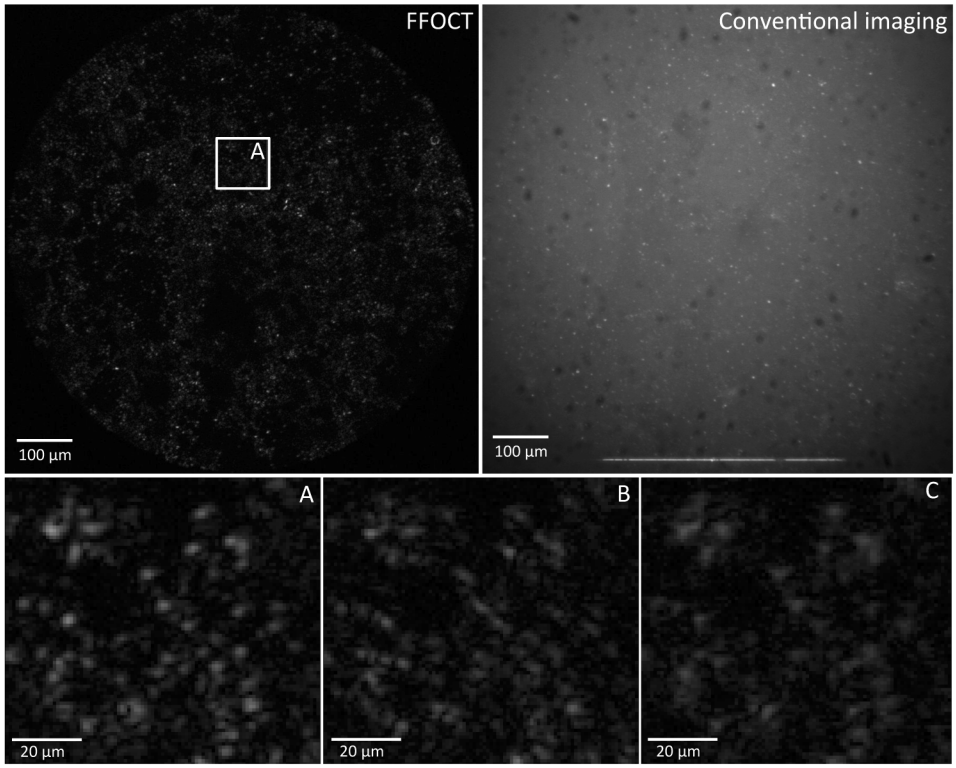

Fig. 5. FFOCT and conventional images of a diffusive painted sample (NEXTEL velvet-coating 811-21) at λ=730 nm. Top; the entire FOV (diameter: 845 µm) without aberration in FFOCT (left) and conventional (right) imaging. The square area selected for the bottom images (90 µm x 80 µm) is displayed in the FFOCT image. The same sample area is acquired in both images and the FFOCT sectioning is evident: the visible scratch at the bottom of the conventional image is not imaged using FFOCT since it is not in the same plane as the diffusers. Bottom; FFOCT images with (A) no aberration, (B) 0.16 µm astigmatism and (C) 0.11 µm trefoil. Image intensity extends over the entire dynamics of the camera. For A, B, and C, intensities are plotted using the same grey-level scale.

aberrations, which is expected, this width being defined by the numerical aperture of the setup. However, the number of speckles increased significantly in the aberrated images, and the cellulose fiber structures were smeared with regard to the aberration-free image (Fig. 4(A)). In Fig. 4(B), 4(C), and 4(D), fibers in some areas still seem to be resolved. However the resolved fiber areas are different from one image to the other. This demonstrates that aberrations strongly impact the reliability and fidelity of the final image. In addition, we observed a decrease in the contrast, with a reduced maximum intensity and a mean intensity closer to the noise background in the OCT images (Figs. 4(B), 4(C), 4(D)).

5.2. Contrast measurement

The contrast, plotted in Fig. 6, was measured on the FFOCT images of the black diffusing painted sample, as presented in Fig. 5. Different amounts of trefoil were applied to the DM, and the corresponding contrast in the computed OCT image was measured on the N brightest pixels as described in Section 4.3.3. As expected, the contrast decreases with an increase in the aberration amplitude.

Optics EXPRESS

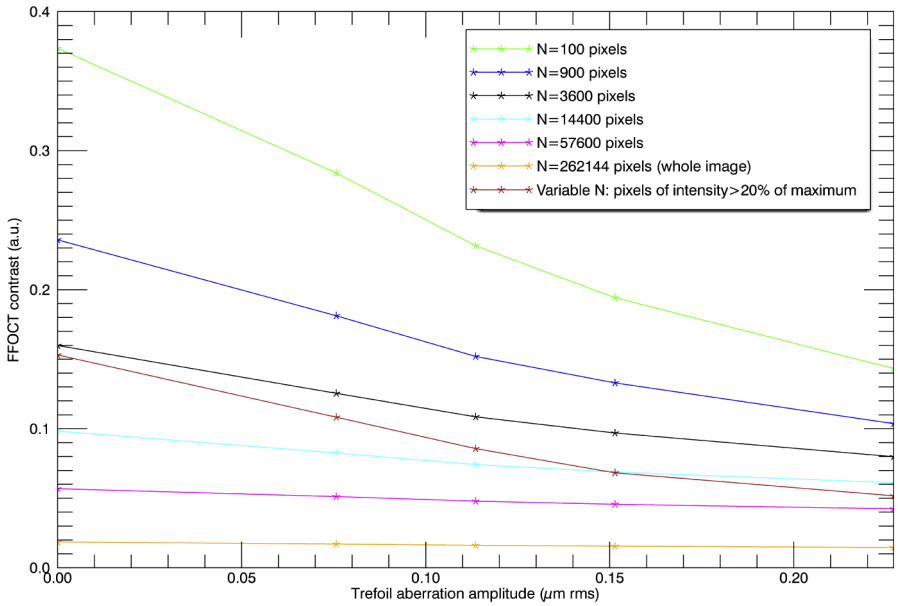

Fig. 6. FFOCT contrast (arbitrary unit) at λ=730 nm versus trefoil aberration amplitude (μm RMS) with a 5 mm pupil for a diffusive painted sample. Light green curve: N=100 pixels; dark blue curve: N=900 pixels; black curve: N=3600 pixels; cyan curve: N=14400 pixels; pink curve: N=57600 pixels; yellow curve: N = 262144 pixels (entire image); garnet red curve for variable number of pixels: pixels of intensity >20% of maximum.

The average contrast of the N brightest pixels was calculated for N ranging between 100 and 262144 pixels (i.e., 512×512). A total of 262144 pixels form the entire image. Thus, the corresponding contrast value is directly linked to the average intensity of the OCT image, dominated by the noise bias value (equal to 0.0125) because the sample is very sparse, with few structures. This bias level was estimated by using the first method for noise calibration described in Section 4.3.1. For a pixel count lower than 4000, the bias level is approximately 0.06, and weak compared to the contrast value. The average contrast of the N pixels with an intensity value greater than 20% of the maximum intensity value in the OCT image was also calculated (garnet red curve).

As expected, all the curves decrease with respect to the aberration amplitude (loss of OCT signal); the contrast is divided by 2.6 for the lowest pixel count. The first value of the curve (on the y-axis, no aberration) decreases when N increases; this is linked to the inclusion of an increasing number of pixels with low-intensity values (until the noise of the entire image is taken into account). The garnet red curve varies between the 3600 pixels curve and the 57600 pixels curve because the number of bright pixels in the computation increases with the aberration amplitude (the signal drops and the noise contribution increases). At large aberrations, the OCT intensity is significantly reduced for all the curves and reaches the noise bias level for the largest number of pixels.

5.3. Resolution measurement

5.3.1. Experimental comparison of resolution loss for conventional and FFOCT images

We utilized a scratch on the diffusive painted plate to analyze the line spread functions (LSF) of different aberrations. In Fig. 7, we present conventional and OCT images for one amplitude of astigmatism (0.42 μm) and without aberration. The enlargement of the scratch image is greater

Optics EXPRESS

in the case of conventional imaging compared to FFOCT. In both cases, it is represented as a duplication of the edges of the scratch. Nevertheless, the enlargement of the OCT image is not symmetric: the secondary edge is dimmer and one can observe oscillations of the intensity (see the following discussion of Fig. 8). As a result, narrow lines are better resolved in the FFOCT aberrated images compared to the incoherent ones.

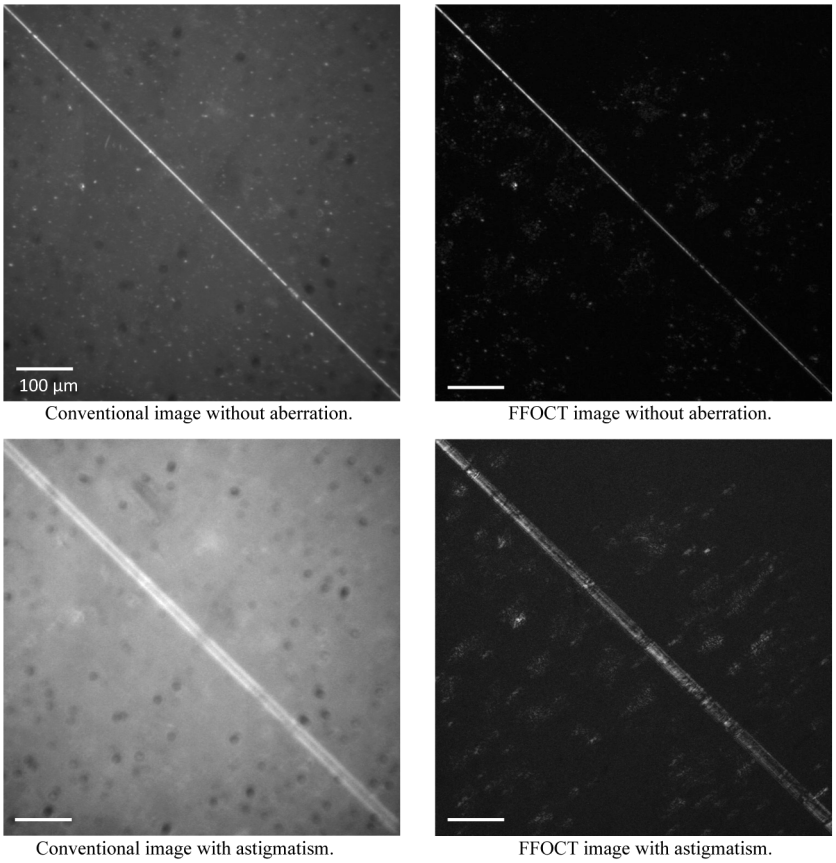

Fig. 7. Images of a scratch on the diffusive painted sample (700 µm × 700 µm) in conventional and FFOCT imaging, without aberration or with 0.42 µm astigmatism. Scale bar: 100 µm.

In Fig. 8, the corresponding raw and normalized profiles perpendicular to the scratch are plotted. The profiles were computed by averaging the pixels along the entire length of the scratch. Changing the scratch portion used to perform the calculations does not alter the results (except that the curves are noisier). Normalization by the maximum was performed after subtracting the minimum value of the profile in the considered window.

For the raw profiles, it is evident that for both imaging processes, the LSF maximum decreases, and the profile is enlarged when the aberration value is increased. The most striking aspect is the stronger decrease of the OCT LSF maximum, which corresponds to the previously mentioned contrast loss. The application of 0.1 µm RMS astigmatism corresponds to a Strehl ratio of approximately 0.48, which is compatible with the results when compared to the green curve (0.1 µm) and the red one (aberration-free best experimental LSF).

For the normalized profiles, the enlargement due to astigmatism is striking in conventional imaging. The OCT LSFs are narrower and present sharper edges than those in conventional imaging. At half maximum, the aberration-free LSF (red curve) is 30% narrower for OCT

Optics EXPRESS

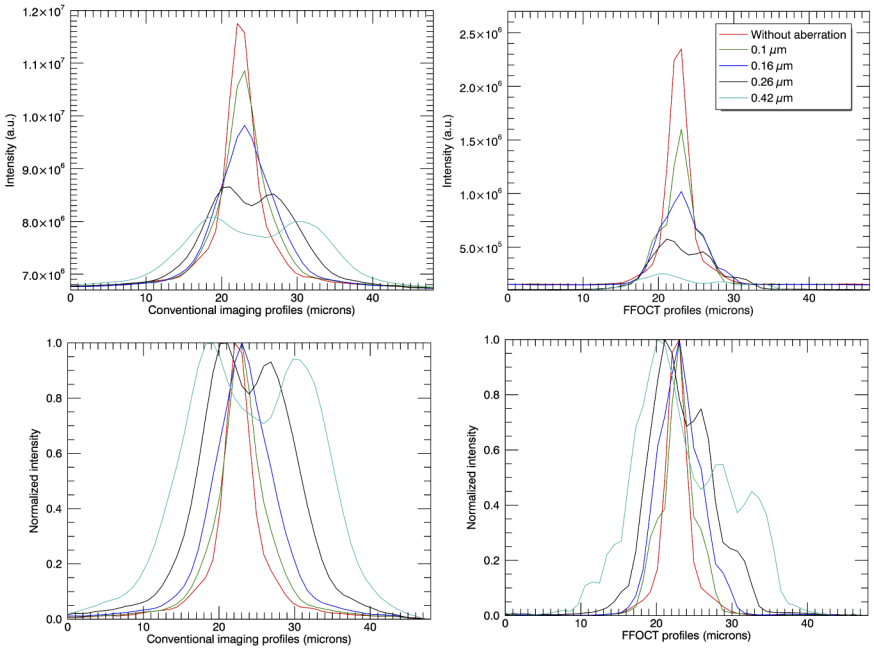

Fig. 8. Raw and normalized profiles of the scratch for FFOCT and conventional images, without aberration and with different astigmatism amplitudes. The red curves represent without aberration. The green curves correspond to the introduction of 0.1 µm RMS astigmatism; dark blue 0.16 µm; black 0.26 µm; cyan 0.42 µm.

compared to conventional imaging: the FWHM for the conventional imaging profile in the object plane is 4.4 µm, whereas that for OCT is 3.1 µm. We observe aberrated OCT LSFs with a main peak surrounded by secondary oscillations: the widening is pronounced at the bottom of the aberrated OCT LSF, whereas its width at half maximum is almost conserved at low levels of aberrations.

We tested other aberrations such as defocus, coma, and trefoil. For all tested aberrations, the FFOCT profiles are distorted in comparison with the narrowest profile without aberration. Depending on the aberration, side lobes (oscillations) appear at the profile basis in OCT LSF and may lead to asymmetrical enlargement. For instance, the introduction of coma creates a deformed component that is prominent along the coma direction. All the FFOCT profiles present similar characteristics for the tested aberrations. We note a global widening in presence of aberrations, with smaller FWHM and sharper edges than in conventional imaging. The signature of the aberrated LSF is made of secondary oscillations, with a structure size in the order of the resolution, and of a central peak broadening slowly with respect to the aberration amplitude and remaining far smaller than the FWHM.

This effect has been investigated by Xiao et al. in [15] for the case of defocus on a gold particle. We mainly confirm their results: we also obtained profiles with an almost constant peak width in their range of amplitudes. Nevertheless, the phenomenon of secondary oscillations is also pronounced with defocus. The OCT LSF is structured, showing the main peak surrounded by oscillations. These artifacts may accentuate the perception of sharp well-resolved objects despite the effective PSF enlargement due to aberrations. Depending on the aberration (PSF with more or less oscillations, asymmetry. . .) and on the object type, the spatial resolution can be preserved (like for a small defocus on a particle) or not.

Optics EXPRESS

5.3.2. Image cutoff frequencies

In the analysis of the resolution of OCT images, we present image spectra, as described in Section 4.3.1. The recorded images were windowed to 512×512 pixels for spectrum computation. First, we define the spatial cutoff frequencies observed in the images. We show in the Appendix that the cutoff frequency for our FFOCT configuration is $\pm 2D$ and not $\pm D$, as is the case in conventional incoherent imaging for an instrument with an aperture diameter equal to D (see also [23,24]). This is associated with the filtering of the object amplitude reflection coefficient in the $\pm D$ domain (and not $\pm D/2$) and the autocorrelation in the spectrum expression due to the square modulus in the OCT image (Eq. (1)).

We show in Figs. 9 and 10 several spectra to demonstrate such cutoff behavior for different pupil diameters without any DM generated aberration. The corresponding images were recorded by adjusting the flux of the illumination source to maintain the photon level per pixel close to the full well capacity regardless of the pupil diameter. Figure 9 corresponds to three spectra acquired for a paper sheet for three different pupil sizes, and for conventional incoherent imaging. The size of the spectra support is 512 pixels and the images were sampled at Shannon for a 7 mm pupil in conventional imaging. The theoretical cutoff frequencies for the 3, 4, and 5 mm pupil diameters are respectively 0.22 μm^{-1}, 0.3 μm^{-1} and 0.37 μm^{-1}, which are experimentally reached for this sample with the available flux. For the three cases, the sample image spectrum reached the noise spectrum floor at the expected cutoff frequency. The different shape for the 5 mm aperture spectrum is probably the signature of possible residual aberrations in the sample arm, which impact the middle-range frequencies for the larger aperture.

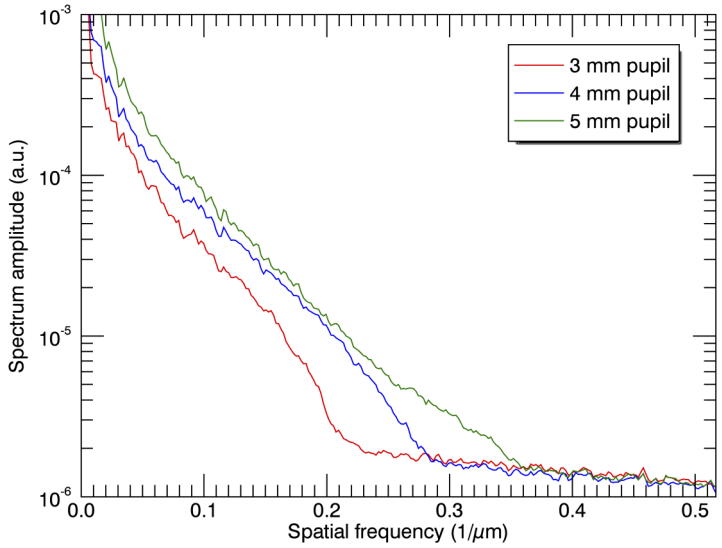

Fig. 9. Image spectra of paper for different pupil sizes in conventional incoherent imaging.

Figure 10 shows the three spectra of the same sample acquired for the three same pupil sizes for FFOCT imaging. It is evident that the FFOCT experimental cutoff frequencies do not correspond to those for incoherent imaging: the FFOCT spectra extend beyond the incoherent imaging cutoff frequency. The FFOCT spectrum has a relatively fast decrease up to the conventional cutoff frequency, whereas for higher frequencies, the decrease appears to be much slower. Theoretically, from Appendix, we expect the cutoff to be 0.44 μm^{-1}, 0.59 μm^{-1} and 0.74 μm^{-1} for the three pupil diameters. The cutoff frequencies for the two largest pupil diameters are not observable because they are higher than 0.52 μm^{-1}, given that the sampling of our setup is not fine enough.

Optics EXPRESS

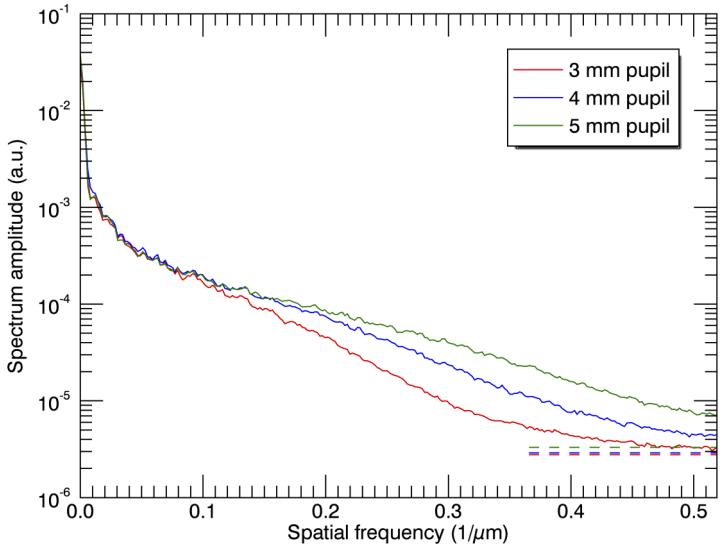

Fig. 10. Image spectra of paper for different pupil sizes in FFOCT imaging. Dash lines: noise spectra at high frequencies estimated using the second method described in Section 4.3.1.

The cutoff is only present in the available frequency range for a diameter of 3 mm. It can be estimated to be approximately 0.45 μm^{-1} when the spectrum reaches the noise plateau, a value close to the expected one. For the two other diameters, we observe that their spectra do not reach the noise plateau in the frequency range of Fig. 10.

The design of our setup did not consider such high cutoff frequencies for the highest pupil diameters. Indeed, the image sampling corresponds to the Shannon condition for a 7 mm aperture in conventional imaging, but not in OCT imaging for pupil diameters larger than 3.5 mm. Therefore, our FFOCT images incur an aliasing effect at the highest frequencies. However, because of the expected decrease of the considered extended object spectra with frequency, this should not be a major issue in our study.

We are now able to compare the spectra computed from both the conventional incoherent images and the FFOCT images.

5.3.3. Image spectra and resolution loss

To quantify the resolution loss due to aberrations, the spatial spectra of the images were computed. In our opinion, defining the resolution as the capability of obtaining a signal at a given spatial frequency above the noise level is appropriate for complex scattering samples, such as those typically encountered in biological imaging. The reduction in contrast at a given spatial frequency directly demonstrates the loss of detail in the image corresponding to this spatial frequency, due to the presence of aberrations.

Figures 11 and 12 show the I_{OCT} spectra and the conventional image spectra, respectively, computed for various RMS wavefront errors of the trefoil for the painted sample. The spectra are truncated on the y-axis to better observe the behavior at high frequencies.

In Fig. 11, we also plot the OCT noise spectra calibrated for each set of aberrations, following the first method given in Section 4.3. We observe that they are all well superimposed as expected, because the number of photons in the interferograms remains nearly constant throughout the experiment regardless of the aberration amplitude. This shows that the plotted spectra in Fig. 11 have the appropriate normalization and can be easily compared to reveal the impact of aberrations.

Optics EXPRESS

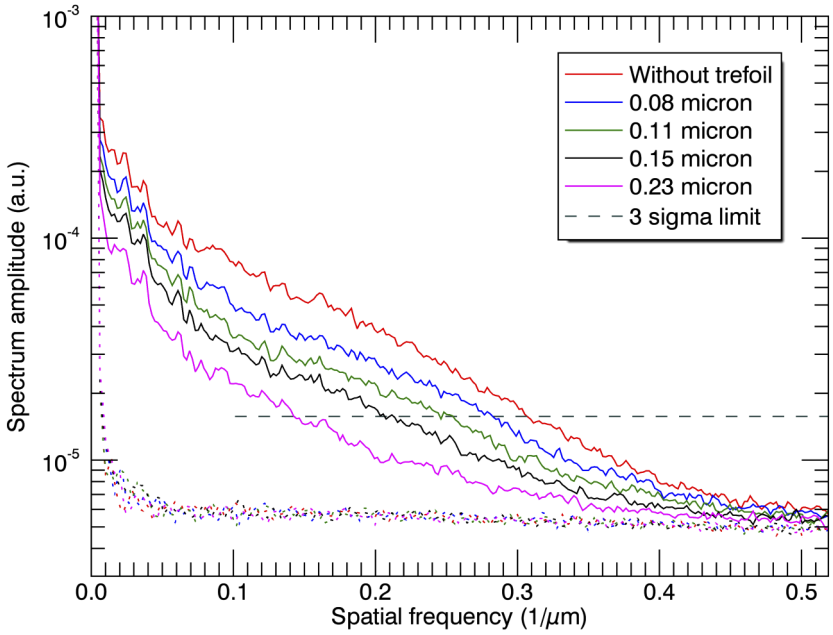

Fig. 11. Spatial spectra of FFOCT images of the painted sample for different amplitudes of trefoil (μm RMS) with a 5 mm pupil. The curves with dotted points characterize the noise spectrum, i.e. the noise level related to each induced aberration. The 3σ limit is also shown.

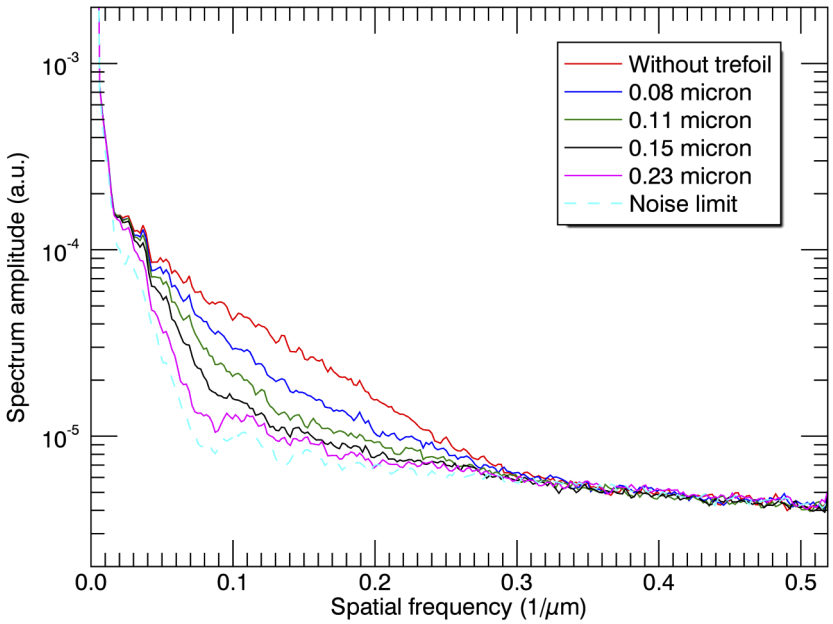

Fig. 12. Spatial spectra of conventional images of the painted sample for different amplitudes of trefoil (micrometers RMS) with a 5 mm pupil.

Optics EXPRESS

We also have to emphasize that on the y-axis of Fig. 11, the value of the spectrum at frequency zero corresponds to the average interferometric contrast value, computed using all the pixels in the OCT image. Increasing the amplitude of the aberration decreases this contrast value (Section 5.2). The computed contrast values for the spectra in Fig. 11 are reported in Table 1. It should be noted that they follow the yellow curve presented in Fig. 6 and are dominated by the noise bias contribution.

Table 1. Contrast values (spectrum value at frequency zero) for the OCT spectra of Fig. 11.

Trefoil value (μm)	Contrast
0	0.0185
0.08	0.0170
0.11	0.0161
0.15	0.0155
0.23	0.0146

The main result given in Fig. 11 is that the frequency content of the OCT images is significantly reduced in the presence of a sufficient level of aberrations. In addition to a reduction of the contrast at the low and middle ranges of the spatial frequencies, we also noticed a change in the shape (change of curvature) of the 0.23 μm trefoil curve (pink curve). This is indicative of an increased impact for the highest amount of aberration on the FFOCT resolution. Indeed, the signal-to-noise ratio at a given frequency in the spectra decreases with an increase in the aberration amplitude. A resolution criterion could consist in being able to detect a given frequency in the OCT image when the spectrum value is at least 3 times higher than the noise level (3σ). This criterion reveals that the higher the frequency, the more difficult is its preservation in an image with a sufficient signal-to-noise ratio. In Fig. 11, the 3σ limit frequency is reduced by a factor of two when applying 0.23 μm trefoil compared to the case without aberration. Considering the highest spatial frequencies, all the curves asymptotically superimpose at the noise level, but this is not observable in Fig. 11 for the available frequency range. The cutoff frequency of the OCT image for the considered pupil should be 0.74 μm^{-1}, which is clearly above the Nyquist frequency (0.52 μm^{-1}) of the computed spectra. It should be noted that the results presented here depend on our experimental conditions and they will be different for another setup. However, regardless of the instrument, it will be used in a given context: biological tissue conditions may limit the amount of flux from the illumination source; the full-well capacity of the camera is also limited; a carefully isolated setup will still remain sensitive to vibrations (limiting the possibility of extensively performing imaging or interferogram averaging); scattering properties are specific to each sample and so on. All these limitations set the noise level at a given value for every setup, but noise will always be present. The useful signal is the one that is above the noise level. This consideration led us to choose a definition of resolution, which takes noise presence into account.

For conventional imaging, the noise spectrum is calibrated from a strongly defocused image of the sample. The translation of the object is approximately 10 mm (enough to get out of the depth of field of the objective). In this case, we are not able to completely suppress the signature of the non-uniformity of the illumination. Therefore, the "noise" spectrum still includes the corresponding low frequencies. Nevertheless, it allows us to evaluate the level of noise in the high-frequency range where all the curves are superimposed. The theoretical cutoff frequency for this pupil size (5 mm) is 0.37 μm^{-1}. We observe in Fig. 12 that all the spectra reach the noise spectrum before this cutoff frequency. The impact of aberrations on conventional imaging is strong and clearly observed in the middle frequency range, with a significant loss of contrast and a change of curvature compared to the case without aberration. Comparing the results of Fig. 11 and 12, we can conclude that due to the doubling of the cutoff frequency and the relatively low

Optics EXPRESS

noise level in the FFOCT images, the frequency content is much higher compared to conventional imaging under the same experimental conditions.

In Fig. 13, we present an example of FFOCT spectra derived from another sample (paper sheet) when applying another aberration to the deformable mirror (astigmatism). It is evident in this sample that the signal-to-noise ratio is higher (stronger reflection coefficient). Given that the pupil size is still 5 mm, the cutoff frequency is not observable. Nevertheless, similar conclusions can be drawn for the significant loss of contrast in the middle and high-frequency range when the amplitude of the aberration is increased. This demonstrates that our conclusions are not dependent on the choice of the sample or the applied aberration.

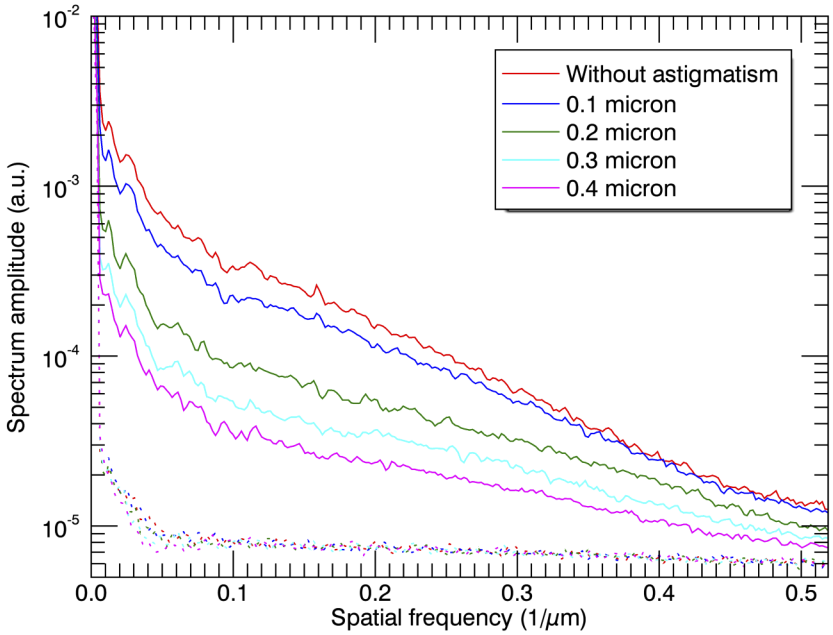

Fig. 13. Spatial spectra of FFOCT images of the paper sample with different amplitudes of astigmatism (micrometers rms). Curves in dotted points characterize the noise spectrum, i.e. the noise level related to each induced aberration.

5.3.4. Discussion

From the image spectra presented in Figs. 11 and 12, we can conclude that the frequency content in an OCT image is much higher than compared to a conventional image because the cutoff frequency is doubled. In addition, the signal-to-noise ratio per frequency is much higher, at least for the experimental conditions used. This demonstrates the peculiar behavior of the spatial resolution and, therefore, the great interest in the FFOCT technique. The doubling of the frequency range is a specific feature of FFOCT, which is already detailed in [23,24]. This does not mean that the aberrations have a low impact on the OCT image, as shown in Fig. 11. We demonstrate that the signal-to-noise ratio at a given frequency is reduced with an increase in the aberration. However, the perception of fine structures (corresponding to high spatial frequencies of the spectra) in the sample is partially preserved even when significant aberrations are introduced. This is emphasized in Figs. 7 and 8, where we notice oscillations around a narrow core of the LSF computed from the images of a scratch.

These observations may explain the conclusions recently reported by Xiao et al. [15] based on experimental images. They showed an image profile on a gold particle with defocus. In this

Optics EXPRESS

case, as we have the same width at half maximum and relatively low sidelobes, the FFOCT image is similar with or without aberration [16]. In the case of a simple sample and medium aberration amplitude, the resolution seems to be maintained; visually, the FFOCT images are of high quality. In the case of *in vivo* retinal imaging, Xiao et al. showed that it is possible to obtain images of resolved photoreceptors of a healthy subject at 6° eccentricity using their FFOCT setup [17]. The quality of these images was comparable to that of images obtained using AO. Photoreceptors are quasi point-like backscatterers, displaying "nice" reflective properties and a quasi-punctual response compared to other retinal structures. At this eccentricity, their density is low, corresponding to a cone spacing of approximately 9 µm [25]. The PSF required to resolve them does not need to be of very high quality. This point is illustrated in Fig. 5, in which the punctual scatterers are well-separated and thus resolved. However, their image, that is, the PSF, is deformed, revealing the signature of the introduced aberration (Figs. 5(B) and 5(C)). More recently, impressive *in vivo* images of photoreceptors were obtained using FFOCT without AO at different eccentricities down to 1.5°, for an area in which the photoreceptor density is still lower compared to the foveola [18]. Nevertheless, ocular aberration values are not clearly specified. It can be supposed that they were weak, as the subject was young and healthy, and wore corrective glasses. This minimized the amount of aberration. These results show that FFOCT may yield high-contrast images when the aberration amplitudes are low and the sample is mainly composed of well-separated quasi-punctual backscatterers. Additionally, we note that resolved cone images have already been obtained at small eccentricities in flood-imaging systems without adaptive optics [26]. However, FFOCT clearly improves the image quality [18].

In this work, we demonstrate that in the presence of aberrations, the image quality of FFOCT is degraded, and the resolution is not maintained for complex samples in which scatterers are not isolated. Due to the convolution process in the image formation, the side lobes of the PSF of neighboring scatterers strongly overlap, degrading the image quality and resolution. These effects are evident in the example of the paper sheet (Fig. 4) and can also be observed in the Fourier plane by the high-frequency wing attenuation (Fig. 13). This is significant at high aberration amplitudes because of the lower signal-to-noise ratio for the highest spatial frequencies, as observed in Fig. 11 for the painted sample. If a high fidelity of the image is expected, we can consider the requirement to achieve at least a 3σ level for the image spectrum compared to the noise level in the spatial frequency domain of interest. In Fig. 11, we note that the frequency domain where this criterion is achievable is dependent on the amplitude of the aberrations. Such a criterion as an image quality metric may assist the designers of FFOCT instruments considering the achievable performance. The performance depends on the experimental constraints, such as the tolerable light flux for *in vivo* tissues, the reflective properties of the sample, and the full well capacity of the imaging camera. In our approach, the spatial resolution is then given by the value of the spatial frequency limit where the 3σ criterion is fulfilled.

6. Conclusion

In this report, we present our theoretical and experimental analysis of the impact of aberrations in FFOCT imaging with regard to conventional incoherent imaging.

Our instrumentation setup coupling adaptive optics and FFOCT was originally meant to provide physicists and ophthalmologists with a modular instrument for 3D high-resolution imaging of the living retina. The instrument is a Linnik interferometer. In the sample arm, the deformable mirror is located in a pupil plane that is conjugated to the exit pupil of the microscope objective (in the case of *ex vivo* studies) and the lenslet array of a Shack-Hartmann wavefront sensor. The pupil in each interferometer arm is tunable in size, allowing for the exploration of several spatial frequency coverages. To observe the impact of the selected aberrations, we used the first-order Zernike polynomials, which were introduced using a calibrated deformable mirror. Their chosen amplitudes were between 0 and a few hundreds of nanometers, comparable with measurements

Optics EXPRESS

made on pathological or aging eyes. The introduced aberrations were achromatic. Using this configuration, we were able to experimentally validate two results, which were also confirmed in the analytical calculations.

First, the cutoff frequency of the instrument is doubled for FFOCT imaging compared to the theoretical value for conventional incoherent imaging. In addition, we observed that the signal-to-noise ratio in the spectrum is much higher in FFOCT compared to wide-field conventional imaging under the same experimental conditions. Both effects result in a higher frequency content in the FFOCT images. Second, aberrations blurred the OCT images for the tested complex samples. This led to the expected loss of contrast, which reduced the signal-to-noise ratio in the image. This also led to a loss in resolution, given that the spatial frequency spectrum was significantly filtered. The attenuation of the image spectrum can result in a low signal-to-noise ratio per frequency, well below the theoretical cutoff. For the diffusive painted sample as an example, the 3σ limit frequency was reduced by a factor of 2 when 0.23 μm trefoil was introduced.

Aberrations negatively affect the FFOCT PSF by creating lateral oscillations around the central peak, while for conventional imaging, the PSF is mainly broadened. For point-like objects, this results in the preserved perception of a high resolution for FFOCT. However, this perception is not achieved in more complex samples, as presented in this report. This is because of the convolution of the sample by the structured PSF, producing numerous random speckles in the obtained image. Moreover, the frequency content is clearly reduced for aberrations of high amplitude. Therefore, in these cases, an aberration compensation system, such as adaptive optics, is required to significantly improve the image quality.

Appendix

In this appendix, we establish the approximate equations that allow us to understand the full-field OCT signal measured using our experimental bench. Here, we will not compute a general expression to model the full 3D scattering process in the sample, as recently reported [24]. Instead, we only consider the surface interaction of the incident light with the sample. To derive the OCT image expression, we follow the principle of microscopy given by Sentenac & Mertz [23].

We define E_0 as the field originating from the sample (the object to be imaged) and incident at the point of coordinate x_1 in the image detector plane as:

$$E_O(x_1, x_0, x) = S(x)A_E(x_0 - x)O(x_0)A_S(x_1 - x_0), \tag{13}$$

where:

- *S(x)* is the field emitted by a source point at coordinate x. This source is assumed to be spatially incoherent and to randomly emit photons,
- $A_E(x_0 - x)$ the unitary diffracted field amplitude that illuminates the object at the point x_0 for a source point at coordinate x, The illumination aperture is in the sample arm, *and* $A_E(x_0 - x)$ is affected by the aberrations of this arm.
- $O(x_0)$ is the reflection coefficient of the amplitude for the scattering object point at x_0,
- $A_S(x_1 - x_0)$ is the unitary diffracted field amplitude at the image point of coordinate x_1 for the wave scattered by the object point at coordinate x_0. This amplitude is also affected by the aberrations of the sample arm.

All the coordinates used are those of the corresponding conjugate points in the image detector plane.

Optics EXPRESS

We write $I(x_1,x_0,x)$ as the observed intensity at position x_1 for a source point and a scattering object point in the detector plane as:

$$I(x_1, x_0, x) = \left\langle |E_O(x_1, x_0, x) + E_R(x_1, x)|^2 \right\rangle, \tag{14}$$

with $E_R(x_1,x)=S(x)A_R(x_1 - x)$, where E_R is the field at position x_1 originating from the reference arm of the interferometer equipped with a perfect mirror for a source point at coordinate x, and $A_R(x_1-x)$ is the corresponding unitary field amplitude (mirror reflection coefficient is assumed to be equal to 1); $|E^2|$ is the square norm of field E and is the expected value of the random variable I over the photon statistics. In OCT, only the cross term in the development of Eq. (14) is of interest $2<Re(E_O E_R^*)> = 2Re<E_O E_R^*>$. Indeed, to extract the object image, OCT signal processing involves the recording of 4 fringe images, each phase-shifted by 0, $\pi/2$, π, and $3\pi/2$, to be used in Eq. (1). This allows us to compute the OCT image as

$$I_{OCT}^2(x_1, x_0, x) = 16\left|\left\langle E_O E_R^* \right\rangle\right|^2. \tag{15}$$

Using the expressions of E_0 and E_R, since the only random variable is $S(x)$, we obtain

$$I_{OCT}^2(x_1, x_0, x) = 16 I_S^2(x)|A_E(x_0 - x)O(x_0)A_S(x_1 - x_0)A_R^*(x_1 - x)|^2, \tag{16}$$

where we define the mean intensity of the source as:

$$I_S(x) = \left\langle |S(x)|^2 \right\rangle. \tag{17}$$

We now compute the full-field OCT image with a 2D scattering object and an extended source illumination. The total field originating from the reference arm is the integral of the source:

$$E_R(x_1) = \int S(x)A_R(x_1 - x)dx. \tag{18}$$

The total field originating from the object is the integral on the object, taking into account the coherence of the illumination through A_E and on the source:

$$E_O(x_1) = \int \left(\int A_E(x_0 - x)O(x_0)A_S(x_1 - x_0)dx_0 \right) S(x)dx. \tag{19}$$

Hence, the general expression of the OCT image in this case using Eq. (15) and the hypothesis of a spatially incoherent source is

$$I_{OCT}^2(x_1) = 16\left| \int \left(\int^{A_E} (x_0 - x)O(x_0)A_S(x_1 - x_0)dx_0 \right) I_S(x)A_R^*(x_1 - x)dx \right|^2, \tag{20}$$

which can be rewritten to reveal a formulation that is close to a convolution between the object and a response function linked to the source and the instrument:

$$I_{OCT}^2(x_1) = 16\left| \int \mathcal{S}(x_1, x_0)A_S(x_1 - x_0)O(x_0)dx_0 \right|^2, \tag{21}$$

where we have identified a term $S(x_1,x_0)$ in the response function that is linked to the source and defined by:

$$\mathcal{S}(x_1, x_0) = \int I_S(x)A_E(x_0 - x)A_R^*(x_1 - x)dx. \tag{22}$$

Equation (21) is the basic equation that defines the FFOCT image given in Eq. (4). This shows that the image of the object is blurred by the response function. The aberrations of the instrument

Optics EXPRESS

have an impact on the OCT image of the object. This impact is driven by A_S and S, which is a more complex term. However, at the limit when A_R is assumed to be close to a Dirac function, we obtain:

$$\mathcal{S}(x_1, x_0) = I_S(x_1)A_E(x_0 - x_1), \tag{23}$$

which reveals a possible impact of A_E similar to that of A_S in the OCT image. Both A_E and A_S are affected by the aberrations in the sample arm.

Let us now investigate the spatial frequency coverage of the full-field OCT. To do this, we approximate Eq. (21) as the convolution product. This assumption is based on the experimental setup in which the illumination source is uniform and extended compared to the width of the diffracted amplitudes A_E and A_R. If we neglect the impact of the border of the illumination on the image, which is windowed to its central part in any case, we can take I_S out of the integral in S. The FFOCT image can be rewritten as

$$I^2_{OCT}(x_1) \approx 16|\mathcal{S}A_S \circledast O|^2, \tag{24}$$

Where $\circledast$ is the symbol for the convolution product.

Taking the Fourier transform (FT) of Eq. (24), we obtain

$$FT(I^2_{OCT}) = 16FT(|\mathcal{S}A_S \circledast O|^2) = 16(FT(\mathcal{S}A_S \circledast O) \otimes FT(\mathcal{S}A_S \circledast O)), \tag{25}$$

where $\otimes$ is the symbol for the correlation product. Thus, we can write:

$$FT(\mathcal{S}A_S \circledast O) = (FT(\mathcal{S}) \circledast FT(A_S))FT(O). \tag{26}$$

The FFOCT image spectrum $FT(I^2_{OCT})$ is the autocorrelation of the object amplitude spectrum $FT(O)$ filtered by $FT(S) \circledast FT(A_S)$. The FT of the response function SA_S is similar to an optical transfer function. Due to the autocorrelation, the frequency support of the OCT image spectrum is twice that of $FT(S) \circledast FT(A_S)$.

We can recognize that:

$$\mathcal{S}(x_1) = I_S(A_E \otimes A_R)(x_1), \tag{27}$$

$$FT(\mathcal{S}) = I_S FT(A_E)FT^*(A_R). \tag{28}$$

The frequency support of $FT(S)$ is imposed by the two filters provided by $FT(A_E)$ and $FT^*(A_R)$, that is, ±D/2 for a pupil diameter D in both the reference and sample arms. Given that the "optical transfer function" $FT(S) \circledast FT(A_S)$ is the convolution product, its frequency support is the sum of the supports of the functions $FT(S)$ and $FT(A_S)$ (that is ± D/2 each), so this sum is ± D. Hence the spatial frequency support of the OCT image spectrum $FT(I^2_{OCT})$ is ±2D, as previously outlined in the literature [23,24].

We can compare this derivation to the one for a conventional image for incoherent illumination of a sample. The field in the detector plane is given by Eq. (19). The conventional image is simply written as $I(x_1) = \langle |E_0(x_1)|^2 \rangle$, which gives:

$$I(x_1) = \int \left(\int^{I_S} (x) |A_E(x_0 - x)|^2 dx \right) |O(x_0)|^2 |A_S(x_1 - x_0)|^2 dx_0. \tag{29}$$

As expected, we recognize the convolution product of the object intensity distribution, including the illumination of the source, and the well-known point spread function of the instrument $|A_S(x_1 - x_0)|^2$. In this case, the illuminated object spectrum is filtered by the optical transfer function, and the frequency support of the conventional image is ± D, as usual.

To better understand the results, let us consider the object amplitude reflection coefficient $O(x_0)$ with only two spatial frequencies f_1 and f_2 such that $f_1 < D/2 < f_2 < D$ and $f_1 + f_2 > D$. In a conventional image, due to filtering by the optical transfer function, we can detect two frequency components of the object intensity distribution: $2f_1$ and $f_2 - f_1$. In the full-field OCT image, we will detect two other components, $2f_2$ and $f_2 + f_1$, attenuated by the filtering process.

Optics EXPRESS

Funding. Région Ile de France (I 06-265 R); Agence Nationale de la Recherche (ANR-10-IDEX-0001-02 PSL*); Centre National de la Recherche Scientifique.

Acknowledgements. This work was initiated in the framework of the MIVOA project (supported by ANR-10-IDEX-0001-02 PSL*) and was supported by Action Spécifique Haute Résolution Angulaire (ASHRA) of CNRS/INSU co-funded by CNES. The instrument development was mainly supported by the project "Rétinopathies" from Région IIe de France, France, grant I 06-265 R. The authors wish to thank Claude Boccara, Serge Meimon, and Frédéric Cassaing for fruitful discussions.

Disclosures. The authors declare no conflicts of interest related to this article.

References

1. D. Huang, E. A. Swanson, C. P. Lin, J. S. Schuman, W. G. Stinsin, W. Chang, M. R. Hee, T. Flotte, K. Gregory, C. A. Puliafito, and J. G. Fujimoto, "Optical coherence tomography," Science **254**(5035), 1178–1181 (1991).
2. J. G. Fujimoto, M. E. Brezinski, G. J. Tearney, S. A. Boppart, B. E. Bouma, M. R. Hee, J. F. Southern, and E. A. Swanson, "Optical biopsy and imaging using optical coherence tomography," Nat. Med. **1**(9), 970–972 (1995).
3. A. F. Fercher, "Optical coherence tomography," J. Biomed. Opt. **1**(2), 157–173 (1996).
4. P. Mecê, E. Gofas-Salas, C. Petit, F. Cassaing, J.-A. Sahel, M. Paques, K. Grieve, and S. Meimon, "Higher adaptive optics loop rate enhances axial resolution in non confocal ophthalmoscopes," Opt. Lett. **44**(9), 2208–2211 (2019).
5. D. R. Williams, "Imaging single cells in the living retina," Vision Res. **51**(13), 1379–1396 (2011).
6. M. Glanc, E. Gendron, F. Lacombe, D. Lafaille, J.-F. Le Gargasson, and P. Léna, "Towards wide-field retinal imaging with adaptive optics," Opt. Commun. **230**(4-6), 225–238 (2004).
7. H. W. Babcock, "The possibility of compensating astronomical seeing," Publ. Astron. Soc. Pac. **65**(386), 229–236 (1953).
8. G. Rousset, J. C. Fontanella, P. Kern, P. Gigan, F. Rigaut, P. Léna, C. Boyer, P. Jagourel, J. P. Gaffard, and F. Merkle, "First diffraction-limited astronomical images with adaptive optics," Astron. Astrophys. **230**, 29–32 (1990).
9. R. Foy and A. Labeyrie, "Feasability of adaptive telescope with laser probe," Astron. Astrophys. **152**, 29–31 (1985).
10. E. Beaurepaire, A. C. Boccara, M. Lebec, L. Blanchot, and H. Saint-Jalmes, "Full-field optical coherence microscopy," Opt. Lett. **23**(4), 244–246 (1998).
11. M. Blavier, L. Blanco, M. Glanc, F. Pouplard, S. Tick, I. Maksimovic, L. Mugnier, G. Chenegros, G. Rousset, F. Lacombe, M. Pâques, J.-F. Le Gargasson, and J.-A. Sahel, "Adding the third dimension on adaptive optics retina imager thanks to full-field optical coherence tomography," Proc. SPIE **7163**, 71630G (2009).
12. L. Vabre, A. Dubois, and A. C. Boccara, "Thermal-light full-field optical coherence tomography," Opt. Lett. **27**(7), 530–533 (2002).
13. A. Dubois, L. Vabre, A. C. Boccara, and E. Beaurepaire, "High-resolution full-field optical coherence tomography with a Linnik microscope," Appl. Opt. **41**(4), 805–812 (2002).
14. V. Mazlin, P. Xiao, E. Dalimier, K. Grieve, K. Irsch, J.-A. Sahel, M. Fink, and A. C. Boccara, "In vivo high resolution human corneal imaging using full-field optical coherence tomography," Biomed. Opt. Express **9**(2), 557–568 (2018).
15. P. Xiao, M. Fink, and A. C. Boccara, "Full-field spatially incoherent illumination interferometry: a spatial resolution almost insensitive to aberrations," Opt. Lett. **41**(17), 3920–3923 (2016).
16. P. Xiao, M. Fink, A. H. Gandjbakhche, and A. C. Boccara, "A resolution insensitive to geometrical aberrations by using incoherent illumination and interference imaging," Eur. Phys. J. Spec. Top. **226**(7), 1603–1621 (2017).
17. P. Xiao, V. Mazlin, K. Grieve, J.-A. Sahel, M. Fink, and A. C. Boccara, "In vivo high-resolution human retinal imaging with wavefront-correctionless full-field OCT," Optica **5**(4), 409–412 (2018).
18. P. Mecê, J. Scholler, K. Groux, and A. C. Boccara, "High-resolution in-vivo human retinal imaging using full-field OCT with optical stabilization of axial motion," Biomed. Opt. Express **11**(1), 492–504 (2020).
19. B. Baumann, C. W. Merkle, R. A. Leitgeb, M. Augustin, A. Wartak, M. Pircher, and C. K. Hitzenberger, "Signal averaging improves signal-to-noise in OCT images: But which approach works best, and when?" Biomed. Opt. Express **10**(11), 5755–5775 (2019).
20. R. J. Noll, "Zernike polynomials and atmospheric turbulence," J. Opt. Soc. Am. **66**(3), 207–211 (1976).
21. K. Bessho, D.-U. G. Bartsch, L. Gomez, L. Chen, H. J. Koh, and W. R. Freeman, "Ocular wavefront aberrations in patients with macular diseases," Retina **29**(9), 1356–1363 (2009).
22. R. A. Applegate, W. J. Donnelly, J. D. Marsack, D. E. Koenig, and K. Pesudovs, "Three-dimensional relationship between high-order root-mean-square wavefront error, pupil diameter, and aging," J. Opt. Soc. Am. A **24**(3), 578–587 (2007).
23. A. Sentenac and J. Mertz, "Unified description of three-dimensional optical diffraction microscopy: from transmission microscopy to optical coherent tomography: tutorial," J. Opt. Soc. Am. A **35**(5), 748–754 (2018).
24. U. Tricoli and R. Carminati, "Modelling of full-field optical coherence tomography in scattering media," J. Opt. Soc. Am. A **36**(11), C122–C129 (2019).
25. R. Legras, A. Gaudric, and K. Woog, "Distribution of cone density, spacing and arrangement in adult healthy retinas with adaptive optics flood illumination," PLoS One **13**(1), e0191141 (2018).
26. D. T. Miller, D. R. Williams, G. M. Morris, and J. Liang, "Images of cone photoreceptors in the living human eye," Vision Res. **36**(8), 1067–1079 (1996).